SnO_2-Ti_3C_2 MXene electron transport layers for perovskite solar cells

Lin Yang[a], Yohan Dall'Agnese[a], Kanit Hantanasirisakul[b], Christopher E. Shuck[b], Kathleen Maleski[b], Mohamed Alhabeb[b], Gang Chen[a], Yu Gao[a], Yoshitaka Sanehira[c], Ajay Kumar Jena[c], Liang Shen[d], Chunxiang Dall'Agnese[a,*], Xiao-Feng Wang[a,*], Yury Gogotsi[a,b], Tsutomu Miyasaka[c]

[a] *Key Laboratory of Physics and Technology for Advanced Batteries (Ministry of Education), College of Physics, Jilin University, 2699 Qianjin Street, Changchun 130012, China*

[b] *A. J. Drexel Nanomaterials Institute, and Department of Materials Science and Engineering, Drexel University, Philadelphia, Pennsylvania 19104, United States*

[c] *Graduate School of Engineering, Toin University of Yokohama, 1614 Kurogane-cho, Aoba, Yokohama, Kanagawa 225-8503, Japan*

[d] *State Key Laboratory on Integrated Optoelectronics, College of Electronic Science and Engineering, Jilin University, 2699 Qianjin Street, Changchun 130012, China*

Corresponding Authors

* Chunxiang Dall'Agnese, *E-mail*: chunxiang@dallagnese.fr

* Xiao-Feng Wang, *E-mail*: xf_wang@jlu.edu.cn

Abstract

MXenes, a class of two-dimensional (2D) transition metal carbides and nitrides, have a wide range of potential applications due to their unique electronic, optical, plasmonic, and other properties. Herein, we explore the use of Ti_3C_2 MXene in organic-inorganic lead halide perovskite solar cells (PSCs) due to its metallic conductivity. SnO_2-Ti_3C_2 MXene nanocomposites with different contents of Ti_3C_2 (0, 0.5, 1.0, 2.0, 2.5 wt.‰) were used as electron transport layers (ETLs) in low-temperature processed planar-structured PSCs. Mixing SnO_2 with 1.0 wt.‰ Ti_3C_2 effectively increases the power conversion efficiency (PCE) from 17.23% to 18.34%, whereas the device prepared with pristine Ti_3C_2 as the ETL achieves a PCE of 5.28%. Photoluminescence and electrochemical impedance spectroscopy results reveal that the metallic Ti_3C_2 MXene nanosheets provide superior charge transfer paths, enhancing electron extraction, electron mobility, and decreasing the electron transfer resistance at the ETL/perovskite interface, and thus leading to higher photocurrents. This work proposes a new field of application for MXenes and a promising method to increasing efficiency of solar cells.

Keywords: Ti_3C_2 MXene, electron transport layers, charge transfer, conductivity, perovskite solar cells

Introduction

Since methylammonium lead iodide ($CH_3NH_3PbI_3$) was first reported as a light absorbing material by Miyasaka *et al.* in 2009,[1] organic-inorganic lead halide perovskite solar cells (PSCs) have received widespread attention.[2,3] Owing to the appropriate bandgap, high absorption coefficient, long carrier diffusion lengths, high charge carrier mobility, and low trap density,[4-5] hybrid perovskites present great potential as an efficient, low-cost, large-scale, and flexible materials for photovoltaic technology.[6] In less than a decade, the power conversion efficiency (PCE) of PSCs improved from 3.8% to above 23%, making them competitive with other solar cells that have been developed for decades and approaching the theoretical efficiency of 33.5%.[7,8] Despite the high PCE, a number of challenges still remain, such as limited electron extraction ability of the electron transport layer (ETL), the intrinsic instability of perovskites against environment (e.g., moisture, air, heat and light), low-temperature processability, mass production, etc.[9,10] To solve these issues and progress toward practical application of PSCs, further research is needed.

In the architecture of PSCs, the ETL plays a significant role in suppressing charge recombination and rectifying photocurrent.[11] Many PSCs are based on meso-superstructures with mesoporous TiO_2 as the ETL, which requires a high-temperature sintering process (> 450°C)[12] and restricts its applications in large-area, flexible or wearable devices in spite of the high PCE.[9] In contrast, PSCs with the planar-heterojunction configuration has more potential owing to its relatively easy and low-cost fabrication resulting from the lack of mesoporous TiO_2 layer, where the perovskite

layer is sandwiched between an ETL and a hole transport layer (HTL).[13] Recently, SnO_2 has emerged as a commonly used ETL in planar PSCs due to its low-temperature processability (≤ 200°C), superior electron mobility, and good optical transparency. SnO_2-based PSCs also exhibit good stability in ambient environment.[14-16] Moreover, combining SnO_2 with n-type semiconductors or high-conductivity materials has proven an effective way to further improve the ETL's electrical conductivity and electron mobility, and thus improving the PCE, highlighting that SnO_2-based ETL shows great potential for high efficiency PSCs.[17-19]

In recent years, two-dimensional (2D) materials, especially graphene, have attracted great attention and have been used in PSCs due to their unique optical and electronic properties.[20,21] To date, $CH_3NH_3PbI_3$-based regular (n-i-p type) and inverted (p-i-n type) PSC containing graphene oxide (GO) as charge transport layer were reported to achieve PCEs of 18.19%[22] and 13.8%[23], respectively. Reducing GO has proven an effective method to improve the conductivity of GO and Yeo *et al.* reported the first reduced graphene oxide (rGO)-based inverted $CH_3NH_3PbI_3$ PSC, which reached a PCE of 10.8%.[24] Recently, Jokar *et al.* further improved this system to exceed 16%.[23] Therefore, it can be seen that conductive 2D materials have great potential in PSCs.

2D materials called MXenes offer a higher conductivity than rGO, while absorbing less light in the visible range. MXenes are 2D transition metal carbides and nitrides with a composition of $M_{n+1}X_nT_x$, where M is an early transition metal, X is carbon and/or nitrogen, and T_x indicates the surface termination (usually oxygen- and/or

fluorine-containing species).[25] MXenes have shown outstanding performance in supercapacitor,[26] catalysis,[27] conducting thin films,[28] sensors,[29] and antennas[30] applications due to their high electrical conductivity and hydrophilicity, which enables processing from aqueous solutions.[28] Interestingly, MXene-based electrodes for dye-sensitized solar cells [31] and MXene as additive in perovskite layer for perovskite solar cells [32] were recently proposed. However, the applications of MXenes in solar cells still remain largely unexplored. Furthermore, MXenes have been reported to enhance the electrical conductivity of semiconductors.[33] These aroused our interest in applying MXenes in ETL to enhance the electron collection in PSCs.

Herein, Ti_3C_2 (the most widely studied MXene) nanosheets were used as a conductive additive in the SnO_2 ETL for low-temperature-processed planar $CH_3NH_3PbI_3$ PSCs. ETL films of SnO_2 with different Ti_3C_2 contents (0, 0.5, 1.0, 2.0, 2.5 wt.‰) were prepared by spin-coating the aqueous mixed SnO_2-Ti_3C_2 colloidal solutions onto indium tin oxide (ITO) substrates. Photovoltaic devices were fabricated with an ITO/ETL/$CH_3NH_3PbI_3$/Spiro-OMeTAD/Ag configuration. The results reveal that the proper addition of Ti_3C_2 to the SnO_2 layer can increase the ETL conductivity, which is beneficial for higher short-circuit current density (J_{sc}) and fill factor (FF) values. Compared with the pristine SnO_2, the PCE of SnO_2-Ti_3C_2-based PSC was improved from 17.23% to 18.34%, achieved by addition of 1.0 wt.‰ Ti_3C_2 to the SnO_2 layer, under the standard AM 1.5G (100 mW cm^{-2}) simulated sunlight illumination. The improvement of PCE can be attributed to faster electron extraction, higher electrical conductivity and electron mobility in the ETL. In the meantime, the pristine Ti_3C_2-

based PSC can also achieve a PCE of 5.28%.

Experimental section

Materials

SnO_2 colloid (15 wt.%, ~5 nm) was purchased from Alfa Aesar. Methylammonium iodide (CH_3NH_3I, >99.5%), lead iodide (PbI_2, >99.99%), 2,2',7,7'-tetrakis-(*N,N*-di-*p*-methoxyphenylamino)-9,9'-spirobifluorene (Spiro-OMeTAD, >99.8%) and lithium-bis(trifluoromethanesulfonyl) imide (Li-TFSI, >99%) were obtained from Xian Polymer Light Technology Corp. 4-tert-butyl pyridine (tBP, 96%) was purchased from Macklin. Ultradry anhydrous dimethylformamide (DMF, 99.8%) and *N,N*-dimethyl sulfoxide (DMSO, 99.7%) were obtained from Beijing Infinity Scientific (INFI). For MAX phase synthesis, titanium powder and aluminum powder were purchased from Aladdin. Graphite was purchased from Sigma Aldrich.

Preparation of Ti_3C_2 MXene

First, Ti_3AlC_2 MAX phase was prepared by mixing 7.368 g of titanium powder, 1.523 g of aluminum powder and 1.109 g of graphite together, then sintered at 1650 °C for 2 hours under argon. Ti_3C_2 MXene was prepared by etching Ti_3AlC_2 powder (≈ 400 mesh) in 12 M LiF/9 M HCl solution at room temperature, as described elsewhere.[34] Briefly, 0.8 g of LiF was added to 10 mL of 9 M HCl under continuous stirring for several minutes. Then 0.5 g Ti_3AlC_2 powder was gradually added (over 5 min) to the etchant solution and continuously reacted for 24 h at room temperature. After that, the acidic mixture was washed with deionized water by repeated centrifugation (5 min per cycle at 8000 rpm). After each cycle, the supernatant was poured out and replaced by new deionized water until its pH > 5. Finally, the slurry was placed in ultrasound for 10 min and centrifuged at 3500 rpm for 1 h. A dark-green colloid supernatant solution

containing Ti_3C_2 nanosheets was obtained. To confirm the concentration of Ti_3C_2 dispersion, 10 mL of Ti_3C_2 dispersion were filtered over a cellulose membrane (0.22 μm pore size). After drying and weighing the peeled-off Ti_3C_2 film, the concentration of Ti_3C_2 was then calculated to be 3 mg mL^{-1}.

Preparation of SnO_2-Ti_3C_2 MXene nanocomposites

The SnO_2 hydrocolloid was diluted to the concentration of 3 wt.% (30 mg mL^{-1}) from 15 wt.% by adding deionized water. Then the Ti_3C_2 dispersion was directly mixed with the SnO_2 hydrocolloid according to the experimental ratios (0, 0.5, 1.0, 2.0, 2.5 wt.‰), which were stirred for 5 minutes before using. SnO_2-Ti_3C_2 MXene films were prepared by spin-coating 70 μL of colloids at 3000 rpm for 30 s onto the ITO substrates in air.

Device fabrication

The pre-patterned ITO substrates were cleaned with detergent, deionized water, acetone, alcohol, and isopropanol in ultrasonic bath for 30 min in sequence, then treated with UV ozone for 30 min. ETL was prepared via spin-coating SnO_2 or SnO_2-Ti_3C_2 nanocomposites or Ti_3C_2 hydrocolloids onto the ITO substrates at 3000 rpm for 30 s in air, followed by thermal annealing on a hot plate at 150 °C for 30 min in air and UV ozone treatment for 30 min. The samples were then moved into a glovebox filled with nitrogen, where a perovskite precursor solution was prepared by mixing 1.3 M (242 mg) PbI_2 and 1.3 M (83 mg) MAI in 408 μL DMF/DMSO (4:1 volume ratio) for 60 min. The perovskite layer was prepared by spin-coating its precursor solution (40 μL) at 5000 rpm for 30 s onto the ETL, and injecting chlorobenzene (350 μL) quickly onto the spinning film in 5 s during the spin-coating process. The obtained film was then heated at 100 °C for 10 min. The hole transport material, Spiro-OMeTAD, was dissolved in

chlorobenzene (80 mg mL^{-1}). Then, 10.5 mL of tBP and 15.5 mL of a Li-TFSI solution (510 mg Li-TFSI/1 mL acetonitrile) were added into Spiro-OMeTAD solution. After 5 minutes of stirring, 25 μL of solution was spin-coated at 4000 rpm for 30 s onto the $CH_3NH_3PbI_3$ layer. The samples were left in the dark at room temperature overnight in dry air. Finally, 60 nm thick Ag electrode was thermally evaporated on the top of Spiro-OMeTAD to assemble a complete PSC device.

Thin film characterization

UV/Vis absorption spectra of ETLs on the ITO were recorded using a Shimadzu UV-3100 spectrophotometer over the 300–900 nm wavelength range. Steady-state photoluminescence (PL) were measured on a Shimadzu RF-5301PC spectrophotometer with excitation at 403 nm and the light from the perovskite surface. Time-resolved photoluminescence (TPL) spectra were obtained on a PL spectrometer (Edinburgh Instruments, FLS 920). The X-ray diffraction (XRD) patterns were recorded on Brucker D8 X-ray diffractometer with CuKα radiation (λ = 1.5418 Å) at 25 °C. The data were collected with a 0.02° step size (2θ) for 0.2 s. The highest occupied molecular orbital (HOMO) energy levels of SnO_2 and SnO_2-Ti_3C_2 (1.0 wt.‰) were measured by an integrated ultrahigh vacuum system equipped with multi-technique surface analysis system (VG Scienta R3000) with an excitation energy of 21.218 eV, and were determined by ultraviolet photoelectron spectroscopy (UPS). A field emission scanning electron microscope (Hitachi SU8000) was used to acquire top-view and cross-sectional scanning electron microscope (SEM) images. The transmission electron microscope (TEM) image of SnO_2-Ti_3C_2 (1.0 wt.‰) nanocomposite was recorded using a JEM-2200FS (JEOL).

Device characterization

The current density-voltage (*J-V*) characteristics of solar cells were measured by a computer-controlled Keithley 2400 source meter measurement system with an AM 1.5G filter at an illumination intensity of 100 mW cm^{-2}, as calibrated by a reference monocrystalline silicon solar cell (91150 V Oriel Instruments). The effective area of the cell was defined to be 0.04 cm^2 using a non-reflective metal mask. The external quantum efficiency (EQE) spectra were measured in air under short-circuit conditions using Crowntech QTest Station 1000AD equipped with a 100 W Xe arc lamp, a filter wheel, and a monochromator. Monochromated light was chopped at a frequency of 80 Hz and photocurrents were measured using a lock-in amplifier. The setup was calibrated using a certified silicon reference diode of known spectral response. The electrochemical impedance spectroscopy (EIS) measurements on the devices were carried out by a VSP multi-channel potentiostat (Biologic, France), under the standard AM 1.5G (100 mW cm^{-2}) simulated sunlight illumination at open-circuit potential with the frequency ranging between 1 MHz and 10 Hz. Z-View Analyst software was used to model the Nyquist plots obtained from the impedance measurements.

Results and Discussion

Characterizations of Ti_3C_2 nanosheets and films of SnO_2, SnO_2-Ti_3C_2 and Ti_3C_2

The Ti_3C_2 MXene nanosheets were synthesized by etching the Al layers from Ti_3AlC_2 MAX phase, as represented in Figure 1a. Figure 1b shows the XRD patterns of Ti_3AlC_2 before and after 24 hours of etching. The most intense peak of Ti_3AlC_2 (104) at 38.9° 2θ disappeared, furthermore the (002) peak at 9.5° shifted to about 7°, confirming the topochemical synthesis of Ti_3C_2. Etching of Al layers and delamination leads to formation of Ti_3C_2 2D nanosheets, as shown in SEM and TEM images in Figure 1c and 1d respectively.

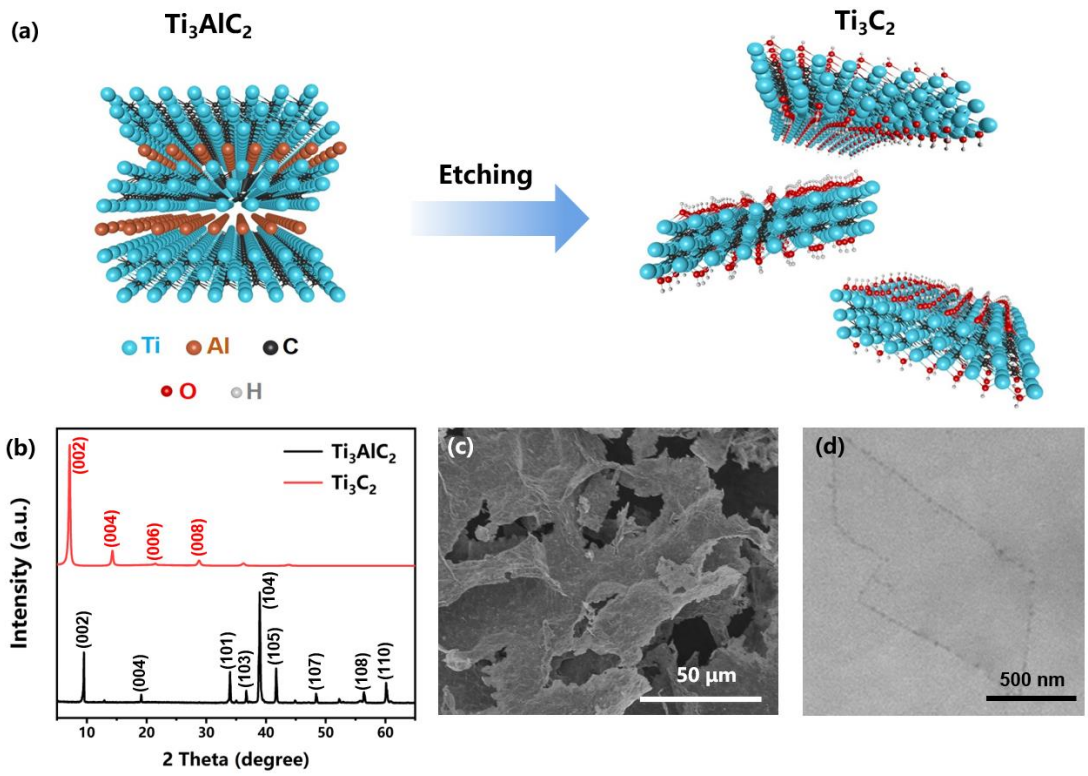

Figure 1. (a) Schematic representation of Ti_3C_2 synthesis, (b) XRD patterns of Ti_3AlC_2 powder and dried Ti_3C_2 film, (c) top-view SEM image of freeze-dried Ti_3C_2, and (d) TEM image of a typical Ti_3C_2 nanosheet.

SnO_2 hydrocolloids containing different amounts of Ti_3C_2 and pristine Ti_3C_2 dispersions are shown in Figure 2a. Because the surfaces of both Ti_3C_2 nanosheets and SnO_2 nanoparticles are negatively charged,[35,36] they do not interact or self-assemble during mixing, and hence, the mixture forms a colloidal suspension in the aqueous medium. Obviously, the color of the colloids became darker along with increasing the concentration of Ti_3C_2 although the amount of Ti_3C_2 is very low (0.5-2.5 wt.‰). For the device fabrication, each suspension was spin-coated at 3000 rpm for 30 s onto ITO-coated glass substrates, followed by thermal annealing at 150 °C for 30 min in air to accomplish ETLs. To investigate the crystal structures, XRD patterns of films spin-

coated from SnO_2, SnO_2–Ti_3C_2 and Ti_3C_2 suspensions on glass were collected (Figure 2b). Because the concentrations of Ti_3C_2 in the nanocomposite samples were too low (1.0 wt.‰) to expect visible peaks, the concentration of Ti_3C_2 was increased 30 times to increase the signal. As shown in Figure 2b, Ti_3C_2 presents a peak at about 7°, corresponding to the (002) diffraction plane. This peak appeared in the SnO_2–Ti_3C_2 diffraction pattern along with all peaks attributed to SnO_2, confirming that the crystal structures of both, Ti_3C_2 and SnO_2, were maintained. This evidenced that the two materials do not undergo any chemical or structural change in the process and coexist in the composite film. Moreover, the high-resolution transmission electron microscope image of SnO_2–Ti_3C_2 (1.0 wt.‰) nanocomposites was shown in Figure S1. SnO_2 nanoparticles can easily to be observed on the surface of Ti_3C_2 nanosheets, indicating successful mixing of SnO_2 and Ti_3C_2.

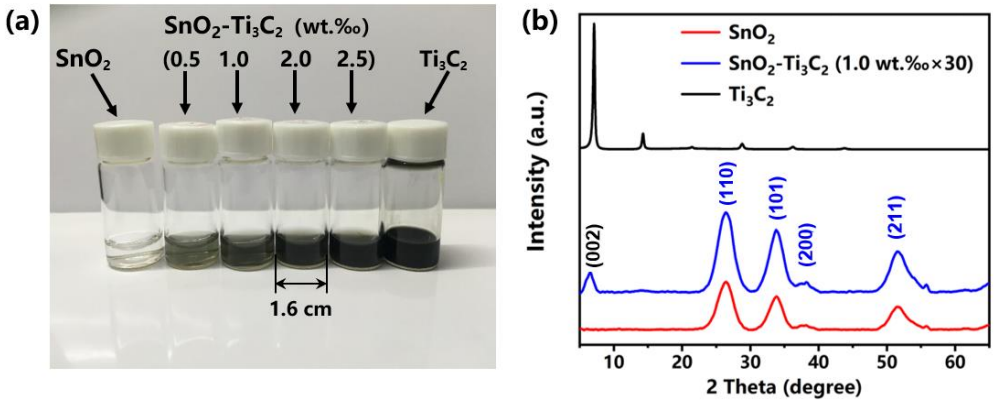

Figure 2. (a) A digital photo of SnO_2 hydrocolloid with different contents of Ti_3C_2 (0, 0.5,1.0, 2.0, 2.5 wt.‰) and Ti_3C_2 dispersion, (b) the XRD patterns of SnO_2, SnO_2–Ti_3C_2 (1.0 wt.‰×30) and Ti_3C_2 films deposited on bare glass substrates.

Photovoltaic characterization

In order to determine the potential of Ti_3C_2 to improve the performance of PSCs, devices with architecture of ITO/ETL/$CH_3NH_3PbI_3$/Spiro-OMeTAD/Ag were fabricated, as presented in Figure 3a. Figure 3b shows a cross-sectional SEM image of the PSC device with the planar architecture. Figure 3c provides the schematic energy-level diagram of each layer, where the HOMO and lowest unoccupied molecular orbital (LUMO) of SnO_2 and SnO_2-Ti_3C_2 nanocomposites are determined by UPS and UV-vis absorption data (see Figure S2 and Table S1). Figure 4a displays the *J–V* curves obtained for PSCs with SnO_2, SnO_2-Ti_3C_2, or Ti_3C_2 as ETLs. Table 1 summarizes the corresponding photovoltaic parameters. Figure S3 shows the PCE histogram of SnO_2-based and SnO_2-Ti_3C_2 (1.0 wt.‰)-based cells, where *J*−*V* parameters display small standard deviation, indicating good reproducibility of devices. It is clear that, with the increase of Ti_3C_2 loading, J_{sc} value continuously increases from 22.83 to 23.56 mA cm^{-2}, accompanied by positive effect on the open-circuit voltage (V_{oc}) and FF in some cases. The optimum performance was obtained with the Ti_3C_2 concentration of 1.0 wt.‰, where V_{oc} and FF reached a maximum, and the PCE went above 18%. We think that metallic Ti_3C_2 flakes function like conductive wires in the composite ETL and offer better electron transport paths, giving rise to more efficient electron collection. As a result, the J_{sc} increases continuously. However, despite J_{sc} kept on increasing, the PCE dropped for higher concentration of Ti_3C_2 (> 1.0 wt.‰), which was apparently due to reduced V_{oc} and FF. In addition, the device with pristine Ti_3C_2 as the ETL demonstrated only 5.28% PCE.

The EQE spectra and integrated currents calculated from them for various ETLs (Figure 4b) are in line with the changes in J_{sc}. The integrated current density from EQE curves for the pristine SnO_2-based cell is 19.62 mA cm^{-2}, and it is increased to 20.2 mA cm^{-2} for the device containing 1.0 wt.‰ Ti_3C_2. The deviation between integrated current from EQE and the actual measured J_{sc} values (Table 1) is about 10%, indicating good accuracy of our *J-V* measured values. Besides, the hysteresis of reverse and forward scans of *J-V* curves is reduced from 17.4% for the device based on pristine SnO_2 to 8.4% for that based on SnO_2-Ti_3C_2 (1.0 wt.‰) (Figure S4).

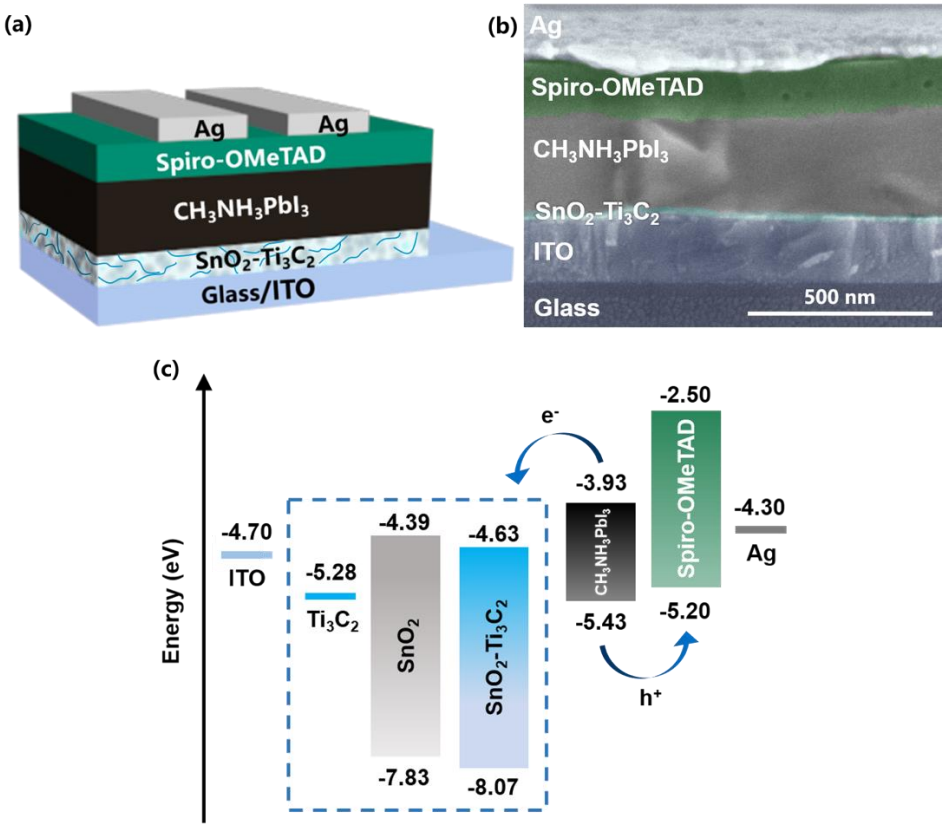

Figure 3. (a) Device architecture of ITO/ETL/$CH_3NH_3PbI_3$/Spiro-OMeTAD/Ag based on representative SnO_2-Ti_3C_2 as ETL, (b) cross-sectional SEM image of the PSC device, and (c) schematic energy-level diagram of each layer.

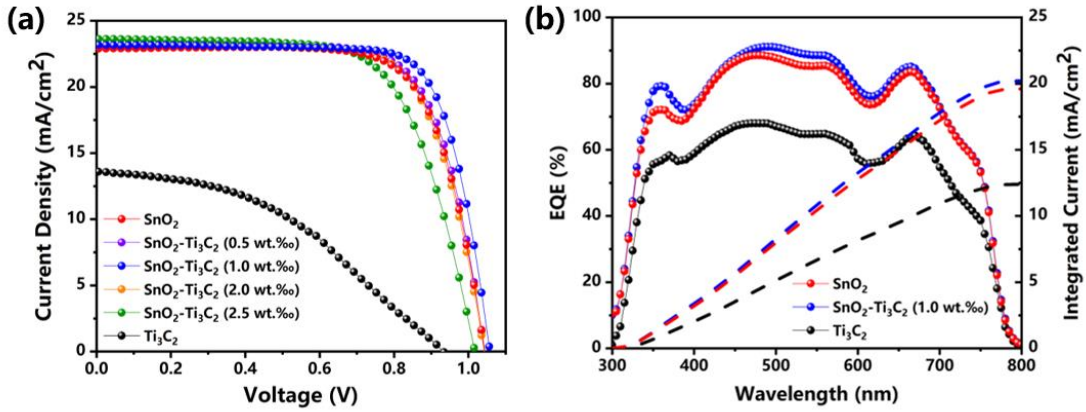

Figure 4. (a) *J-V* curves of PSCs based on SnO_2, SnO_2-Ti_3C_2 (prepared with different concentrations of Ti_3C_2) and Ti_3C_2 as ETLs under AM 1.5G simulated illumination, (b) EQE spectra and the corresponding integrated current densities for the representative PSCs fabricated with SnO_2, SnO_2- Ti_3C_2 (1.0 wt.‰) and Ti_3C_2 respectively.

Table 1. The photovoltaic performance parameters of PSCs based on ETLs under different conditions.

ETL	V_{oc} (V)	J_{sc} (mA cm^{-2})	FF (%)	PCE (%)
SnO_2	1.05±0.01	22.83±0.21	72±0.88	17.23±0.55
SnO_2-Ti_3C_2 (0.5 wt.‰)	1.05±0.01	22.99±0.23	73±0.98	17.56±0.51
SnO_2-Ti_3C_2 (1.0 wt.‰)	1.06±0.01	23.14±0.30	75±0.86	18.34±0.50
SnO_2-Ti_3C_2 (2.0 wt.‰)	1.04±0.01	23.20±0.31	71±0.90	17.22±0.54
SnO_2-Ti_3C_2 (2.5 wt.‰)	1.02±0.01	23.56±0.30	68±0.91	16.34±0.60
Ti_3C_2	0.93±0.02	13.69±0.48	41±1.32	5.28±0.54

To gain insight into the possible reasons for the improvement of PCE upon adding

little amount of Ti_3C_2, $CH_3NH_3PbI_3$ films or devices based on SnO_2, SnO_2-Ti_3C_2 (1.0 wt.‰), and Ti_3C_2 were selected and further investigated. The XRD patterns of $CH_3NH_3PbI_3$ films were recorded and shown in Figure S5a. Here, the $CH_3NH_3PbI_3$ films were prepared on ETL films according to previously reported one-step deposition method,[37] as detailed in the experimental section (see Supporting Information). The XRD result is similar to that previously reported. Figure S5b-d show the SEM images of perovskite layer based on ITO/SnO_2, ITO/SnO_2-Ti_3C_2 (1.0 wt.‰), and ITO/Ti_3C_2, respectively. All the films were pinhole-free with smooth surface and large grains, which are the basis for good performance devices. Indeed, this implied that there was no significant effect of perovskite layer on the device performance difference. The enhancement in cell performance must be related to the ETL instead of perovskite.

Figure S6a displays photographs of SnO_2, SnO_2–Ti_3C_2 (1.0 wt.‰) and Ti_3C_2 films fabricated by spin-coating onto ITO. Both films of SnO_2 and SnO_2–Ti_3C_2 are transparent and there is a little change of the color between them. The film of Ti_3C_2 obviously became dark compared to that of SnO_2 and SnO_2–Ti_3C_2, as expected from the color of their suspensions. Figure S6b-d show their magnified SEM images. The morphologies of the SnO_2–Ti_3C_2 is similar to that of SnO_2, both films are flat, uniform, and pinhole-free, suggesting the corresponding PSCs are likely of the planar-heterojunction configuration. The results are in coherence with the UV-vis absorption spectra of the various films shown in Figure 5a. Precisely, the curves of SnO_2 and SnO_2–Ti_3C_2 films are almost the same, while the Ti_3C_2 curve has a slightly stronger absorption in the UV region (λ = 330 nm), indicating that the addition of Ti_3C_2 to SnO_2 layer does

not affect the transmission of light.

To know the electron extraction abilities of different ETLs, the PL spectra of perovskite absorber layer spin-coated onto ITO/SnO_2, ITO/SnO_2-Ti_3C_2 (1.0 wt.‰) and ITO/Ti_3C_2 substrates were measured, as shown in Figure 5b. The PL quenching is originated from the electron extraction across the interface of $CH_3NH_3PbI_3$/ETL. The PL signal at about 780 nm is assigned to the emission from $CH_3NH_3PbI_3$. ITO/Ti_3C_2/perovskite shows the highest PL intensity, indicating the hole blocking ability of Ti_3C_2 is less good, thus there is more carrier recombination happening in this device. This can be attributed to the metallic nature of Ti_3C_2 whose work function is higher than the valence band edge of $CH_3NH_3PbI_3$ (Figure 3c), The lowest PL intensity is obtained with the ITO/SnO_2-Ti_3C_2 (1.0 wt.‰)/perovskite sample. It is lower than that of ITO/SnO_2/perovskite, indicating the addition of Ti_3C_2 successfully enhanced the electron extraction from perovskite to ETL and suppressed carrier recombination. Figure 5c gives the TPL spectra of perovskites based on different ETLs. The lifetimes of PL decay of SnO_2, SnO_2-Ti_3C_2 (1.0 wt.‰) and Ti_3C_2 –based perovskites are 40.3 ns, 33.8 ns, and 42.7 ns, respectively. This is consistent with the steady-state PL results, further supporting the results from *J–V* curves and EQE spectra, and demonstrating that the addition of Ti_3C_2 to SnO_2 significantly enhances the J_{sc}.

To investigate the changes in FF, which is related to charge collection and conductivity, determined by interfacial charge transfer, EIS characterization was done on the devices with the architecture of ITO/ETL/$CH_3NH_3PbI_3$/Spiro-OMeTAD/Ag,

where the ETL is either SnO_2, SnO_2–Ti_3C_2 (1.0 wt.‰) or Ti_3C_2, under the standard AM 1.5G (100 mW cm^{-2}) simulated sunlight illumination at 0 V relative to the open-circuit potential with the frequency ranging from 1 MHz to 10 Hz. Figure 5d shows the Nyquist plots of the three devices which present semi-circles corresponding to the equivalent circuit model proposed. Here, R_s is the series resistance largely associated with wires and the ITO substrate. The observed major semi-circle represents the charge recombination resistance (R_{rec}) and interfacial capacitance (C) at the ETL/perovskite interface.[38] R_{rec} is inversely proportional to charge recombination, in other words, higher R_{rec} suggests lower carrier recombination (better hole blocking ability). The values fitted to the equivalent circuit are tabulated in Table S2. The value of R_{rec} follows the order SnO_2 > SnO_2–Ti_3C_2 > Ti_3C_2, where the larger resistance is favorable to higher electron collection. Ti_3C_2-based PSC has the lowest R_{rec}, indicating the most charge recombination occurred at the interface, and thus resulting in the lowest FF. This is consistent with *J-V* results. Despite that the PSC based on SnO_2–Ti_3C_2 has lower charge recombination resistance compared to SnO_2, its J_{sc} and FF are larger than the SnO_2-based device. This can be partly attributed to the better electron extraction due to the addition of Ti_3C_2, as reflected in the steady-state PL spectra.

Electron mobility of the ETL was evaluated by the method of space charge-limited current (SCLC) on electron-only devices with the structure of ITO/TiO_2/ETL/BCP/Ag under dark (Figure S7). The highest electron mobility among the three ETLs was determined as 2.23×10^{-5} cm^2 V^{-1} s^{-1} for Ti_3C_2, almost triple that of SnO_2 (7.52×10^{-6} cm^2 V^{-1} s^{-1}). Despite of the high electron mobility of Ti_3C_2, it showed the least efficient

electron extraction and the most charge recombination, as demonstrated by the steady-state PL and EIS results, resulting in its lowest J_{sc} and FF, and thus the lowest PCE. As Ti_3C_2 nanosheets have good conductivity, it is coherent that after introducing Ti_3C_2 in SnO_2 layer, the electron mobility was increased to 1.23×10^{-5} cm^2 V^{-1} s^{-1} in the SnO_2-Ti_3C_2 sample, which is about ten times higher than that of TiO_2 [39]. The mobility results also effectively explain the increase in J_{sc} and FF values in the device based on SnO_2-Ti_3C_2 compared to the one based on SnO_2.

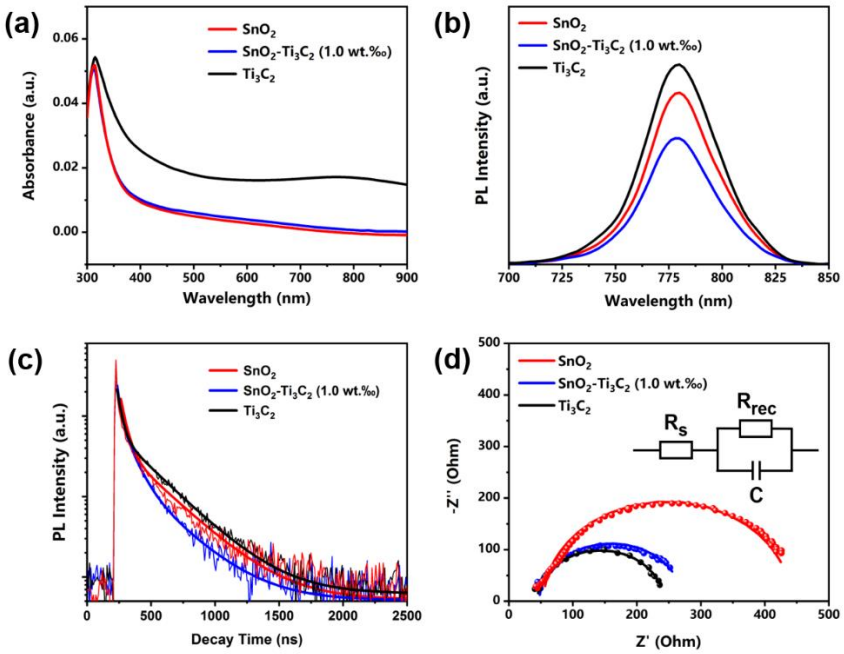

Figure 5. (a) UV-vis absorption spectra of SnO_2, SnO_2-Ti_3C_2 (1.0 wt.‰), and Ti_3C_2 films fabricated by spin-coating onto the ITO substrates, (b) PL (excitation at 403 nm) and (c) TPL spectra of ITO/SnO_2/$CH_3NH_3PbI_3$, ITO/SnO_2-Ti_3C_2 (1.0 wt.‰)/$CH_3NH_3PbI_3$, ITO/Ti_3C_2/$CH_3NH_3PbI_3$, (d) Nyquist plots of the PSCs with SnO_2, SnO_2-Ti_3C_2 (1.0 wt.‰), or Ti_3C_2 as ETLs under one sun illumination, where the scattered points are experimental data and the solid lines are the fitted curves according

to the equivalent circuit.

Apart from the increase of PCE, the effects of adding Ti_3C_2 to SnO_2 ETL on the device stability were also studied. Figure S8 shows the stability results of PSCs based on SnO_2, SnO_2–Ti_3C_2 (1.0 wt.‰) and Ti_3C_2 as ETLs in ambient air (relative humidity ≈20 %) without encapsulation at 25 °C, which were tested under the standard AM 1.5G (100 mW cm^{-2}) simulated sunlight illumination. Despite the pristine Ti_3C_2-based PSC showing a good stability within the first 192 h, an obvious reduction of the PCE occurred after 192 h. On the contrary, PSCs based on SnO_2–Ti_3C_2 and SnO_2 exhibited similar good stability trends for 768 h. SnO_2–Ti_3C_2-based PSC just showed slightly increased and less fluctuating stability compared to the SnO_2-based one, indicating that the addition of Ti_3C_2 had no negative impact on the device stability. Moreover, after 700 hours of storage, the SnO_2–Ti_3C_2-based PSC retained about 80% of the initial PCE, demonstrating the excellent stability of this device.

Conclusion

Conductive Ti_3C_2 MXene nanosheets were prepared and nanocomposites of Ti_3C_2 and SnO_2 were used as the electron transport layers for perovskite solar cells. Flat, uniform and pinhole-free films of SnO_2 containing different amounts of Ti_3C_2 (0, 0.5, 1.0, 2.0, 2.5 wt.‰) were prepared by spin-coating. A relatively high PCE of 18.34% was achieved using SnO_2-Ti_3C_2 (1.0 wt.‰) as the ETL with a device architecture of ITO/ETL/$CH_3NH_3PbI_3$/Spiro-OMeTAD/Ag. The variation of efficiency from cell to cell is smaller than that of graphene-based $CH_3NH_3PbI_3$ PSCs with regular

configuration (15.42±0.54%),[22] highlighting the potential application of MXenes toward the development of low-cost solar cells. This high efficiency originated from an excellent electron extraction, electron mobility and low interfacial charge transfer resistance of the SnO_2-Ti_3C_2 layer, thanks to the good conductivity of Ti_3C_2 MXene which provides charge transfer paths, as evidenced by the steady-state PL spectra, SCLC and EIS results. A PCE of only 5.28% was achieved using pristine Ti_3C_2 as the ETL. This work sets a milestone for incorporation of 2D MXenes into solar cells. Moreover, the fabrication of low-temperature and solution-processed ETL offers prospective applications for flexible photovoltaic devices.

Conflict of Interest

The authors declare no conflict of interest.

Acknowledgements

This work was partially supported by the National Natural Science Foundation of China (No. 11574111 to X.-F.W.) and Natural Science Foundation of Jilin Province (No. 20160101303JC). The authors gratefully thank the College of Physics of Jilin University and the Foreign 1000 Talent plan (China) for financial support.

Supporting Information

SEM and TEM images, UPS analysis, optoelectronic parameters of SnO_2 and SnO_2-Ti_3C_2 (1.0 wt.‰), device reproducibility results, XRD analysis, SCLC results, EIS

fitting parameters, and device stability. This material is available from website at http://..... or from the author.

References

1. A. Kojima, K. Teshima, Y. Shirai and T. Miyasaka, *J. Am. Chem. Soc.*, 2009, **131**, 6050-6051.
2. J. H. Im, C. R. Lee, J. W. Lee, S. W. Park and N. G. Park, *Nanoscale*, 2011, **3**, 4088-4093.
3. J. Burschka, N. Pellet, S. J. Moon, R. Humphry-Baker, P. Gao, M. K. Nazeeruddin and M. Gratzel, *Nature*, 2013, **499**, 316-319.
4. W. J. Yin, T. Shi and Y. Yan, *Adv. Mater.*, 2014, **26**, 4653-4658.
5. S. D. Stranks, G. E. Eperon, G. Grancini, C. Menelaou, M. J. P. Alcocer, T. Leijtens, L. M. Herz, A. Petrozza and H. J. Snaith, *Science*, 2013, **342**, 341-344.
6. Y. Li, L. Meng, Y. M. Yang, G. Xu, Z. Hong, Q. Chen, J. You, G. Li, Y. Yang and Y. Li, *Nat. Commun*., 2016, **7**, 10214.
7. K. A. Bush, A. F. Palmstrom, Z. J. Yu, M. Boccard, R. Cheacharoen, J. P. Mailoa, D. P. Mcmeekin, R. L. Z. Hoye, C. D. Bailie and T. Leijtens, *Nat. Energy*, 2017, **2**, 17009.
8. H. Tsai, W. Nie, J. C. Blancon, C. C. Stoumpos, R. Asadpour, B. Harutyunyan, A. J. Neukirch, R. Verduzco, J. J. Crochet, S. Tretiak, L. Pedesseau, J. Even, M. A. Alam, G. Gupta, J. Lou, P. M. Ajayan, M. J. Bedzyk and M. G. Kanatzidis, *Nature*, 2016, **536**, 312-316.
9. J. M. Ball, M. M. Lee, A. Hey and H. J. Snaith, *Energy Environ. Sci.*, 2013, **6**, 1739-1743.
10. A. D. Sheikh, A. Bera, M. A. Haque, R. B. Rakhi, S. D. Gobbo, H. N. Alshareef and T. Wu, *Sol. Energy Mater. Sol. Cells*, 2015, **137**, 6-14.
11. G. E. Eperon, V. M. Burlakov, P. Docampo, A. Goriely and H. J. Snaith, *Adv. Funct. Mater.*, 2014, **24**, 151-157.
12. M. M. Lee, J. Teuscher, T. Miyasaka, T. N. Murakami and H. J. Snaith, *Science*, 2012, **338**, 643-647.
13. C.-C. Chueh, C.-Z. Li and A. K. Y. Jen, *Energy Environ. Sci.*, 2015, **8**, 1160-1189.
14. W. Ke, G. Fang, Q. Liu, L. Xiong, P. Qin, H. Tao, J. Wang, H. Lei, B. Li, J. Wan, G. Yang and Y. Yan, *J. Am. Chem. Soc.*, 2015, **137**, 6730-6733.
15. J. Song, E. Zheng, J. Bian, X.-F. Wang, W. Tian, Y. Sanehira and T. Miyasaka, *J. Mater. Chem. A*, 2015, **3**, 10837-10844.
16. G. Yang, C. Chen, F. Yao, Z. Chen, Q. Zhang, X. Zheng, J. Ma, H. Lei, P. Qin, L. Xiong, W. Ke, G. Li, Y. Yan and G. Fang, *Adv. Mater.*, 2018, **30**, 1706023.
17. X. Ren, D. Yang, Z. Yang, J. Feng, X. Zhu, J. Niu, Y. Liu, W. Zhao and S. F. Liu, *ACS Appl. Mater. Interfaces*, 2017, **9**, 2421-2429.
18. M. Park, J.-Y. Kim, H. J. Son, C.-H. Lee, S. S. Jang and M. J. Ko, *Nano Energy*,

2016, **26**, 208-215.
19. G. Yang, H. Lei, H. Tao, X. Zheng, J. Ma, Q. Liu, W. Ke, Z. Chen, L. Xiong, P. Qin, Z. Chen, M. Qin, X. Lu, Y, Yan and G. Fang, *Small*, 2017, **13**, 1601769.
20. E. L. Lim, C. C. Yap, M. H. H. Jumali, M. A. M. Teridi and C. H. Teh, *Nano-Micro Lett.*, 2018, **10**, 27.
21. G. Kakavelakis, E. Kymakis and K. Petridis, *Adv. Mater. Interfaces*, 2018, **5**, 1800339.
22. A. Agresti, S. Pescetelli, B. Taheri, A. E. Del Rio Castillo, L. Cina, F. Bonaccorso and A. Di Carlo, *ChemSusChem*, 2016, **9**, 2609-2619.
23. E. Jokar, Z. Y. Huang, S. Narra, C.-Y. Wang, V. Kattoor, C.-C. Chung and E. W.-G. Diau, *Adv. Energy Mater.*, 2018, **8**, 1701640.
24. J. S. Yeo, R. Kang, S. Lee, Y. J. Jeon, N. S. Myoung, C. L. Lee, D. Y. Kim, J. M. Yun, Y. H. Seo and S. S. Kim, *Nano Energy*, 2015, **12**, 96-104.
25. M. Naguib, M. Kurtoglu, V. Presser, J. Lu, J. Niu, M. Heon, L. Hultman, Y. Gogotsi and M. W. Barsoum, *Adv. Mater.*, 2011, **23**, 4248-4253.
26. M. R. Lukatskaya, O. Mashtalir, C. E. Ren, Y. Dall'Agnese, P. Rozier, P. L. Taberna, M. Naguib, P. Simon, M. W. Barsoum and Y. Gogotsi, *Science*, 2013, **341**, 1502-1505.
27. Y. Sun, D. Jin, Y. Sun, X. Meng, Y. Gao, Y. Dall'Agnese, G. Chen and X.-F. Wang, *J. Mater. Chem. A*, 2018, **6**, 9124-9131.
28. A. D. Dillon, M. J. Ghidiu, A. L. Krick, J. Griggs, S. J. May, Y. Gogotsi, M. W. Barsoum and A. T. Fafarman, *Adv. Funct. Mater.*, 2016, **26**, 4162-4168.
29. A. Sinha, Dhanjai, H. Zhao, Y. Huang, X. Lu, J. Chen and R. Jain, *Trends Anal. Chem.*, 2018, **105**, 424-435.
30. A. Sarycheva, A. Polemi, Y. Liu, K. Dandekar, B. Anasori and Y. Gogotsi, *Sci. Adv.*, 2018, **4**, eaau0920.
31. C. Dall'Agnese, Y. Dall'Agnese, B. Anasori, W. Sugimoto and S. Mori, *New J. Chem.*, 2018, **42**, 16446-16450.
32. Z. Guo, L. Gao, Z. Xu, S. Teo, C. Zhang, Y. Kamata, S. Hayase and T. Ma, *Small*, 2018, **14**, 1802738.
33. J. Guo, B. Legum, B. Anasori, K. Wang, P. Lelyukh, Y. Gogotsi and C. A. Randall, *Adv. Mater.*, 2018, **30**, e1801846.
34. M. Alhabeb, K. Maleski, B. Anasori, P. Lelyukh, L. Clark, S. Sin and Y. Gogotsi, *Chem. Mater.*, 2017, **29**, 7633-7644.
35. N. Siedl, S. O. Baumann, M. J. Elser and O. Diwald, *J. Phys. Chem. C*, 2012, **116**, 22967-22973.
36. Y. Ying, Y. Liu, X. Wang, Y. Mao, W. Cao, P. Hu and X. Peng, *ACS Appl. Mater. Interfaces*, 2015, **7**, 1795-1803.
37. M. Li, S.-i. Sasaki, Y. Sanehira, T. Miyasaka, H. Tamiaki, T. Ikeuchi, G. Chen and X.-F. Wang, *J. Photochem. Photobiol. A: Chem*., 2018, **353**, 639-644.
38. A. Pockett, G. E. Eperon, T. Peltola, H. J. Snaith, A. Walker, L. M. Peter and P. J. Cameron, *J. Phys. Chem. C*, 2015, **119**, 3456-3465.
39. J. H. Heo, M. S. You, M. H. Chang, W. Yin, T. K. Ahn, S.-J. Lee, S.-J. Sung, D. H. Kim and S. H. Im, *Nano Energy*, 2015, **15**, 530-539.